water

MDPI

Article

On the Usefulness of the Proper Orthogonal Decomposition on the Description of the Highly Concentrated Sediment Release Phenomena Resulting from a Two-Phase Solid-Fluid Simulation: Effect of the Ambient Current

Alina Santa Cruz [1], Duc Hau Nguyen [2] and Sylvain S. Guillou [1,*]

[1] Laboratoire Universitaire des Sciences Appliquées de Cherbourg (LUSAC, UR 4253), Université de Caen Normandie, 60 rue Max Pol Fouchet CS 20082, 50130 14000 Caen, France; alina.santa-cruz@unicaen.fr
[2] Faculty of Computer Science and Engineering, Thuyloi University, C5, 175 Tay Son St., Hanoi 116705, Vietnam; ndhau.dhtl@tlu.edu.vn
* Correspondence: sylvain.guillou@unicaen.fr; Tel.: +33-2-33-01-40-32

Abstract: Proper orthogonal decomposition (POD) is used to examine the release of highly concentrated water–sediment mixture in water, with or without ambient current. This technique allows us to extract the dominant features in spatio-temporal data sets and the POD total energies associated to the base parameter of the decomposition. Both one-component and two-component POD techniques are, respectively, applied on data relative to the solid volume fraction and on the solid volume fraction velocities. The analysis is based on an experiment in the literature and data sets provided by a two-phase flow solid-fluid numerical simulation. For release phenomenon without ambient current, the analysis of the POD results highlights that the impact of the particle diameter on the solid phase dynamics and the particle dispersion is modest during the falling time, but that it becomes preponderant during the formation of a turbidity current. Aided by POD, the impact of the ambient current is studied for a given particle diameter. As the ambient current becomes strong, we can observe the effect of the resistance of the bottom against the water–sediment mixture transport. According to the strength of the ambient current, the POD results show that the dynamics of the release phenomenon have two different regimes on either side of a clearly identified threshold value.

Keywords: dredged sediment release; sediment transport; two-phase flow modelling; fine sand; snapshot proper orthogonal decomposition (POD)

Citation: Santa Cruz, A.; Nguyen, D.H.; Guillou, S.S. On the Usefulness of the Proper Orthogonal Decomposition on the Description of the Highly Concentrated Sediment Release Phenomena Resulting from a Two-Phase Solid-Fluid Simulation: Effect of the Ambient Current. *Water* **2023**, *15*, 3284. https://doi.org/10.3390/w15183284

Academic Editor: Achim A. Beylich

Received: 17 July 2023
Revised: 7 September 2023
Accepted: 9 September 2023
Published: 18 September 2023

1. Introduction

The maintenance and increase in the water depth is necessary to ensure a safe entrance to navigation channels, harbors, and docks. Dredging operations are a routine necessity to remove the sediments and debris gradually carried into the different passage zones of the ships. The dredged sediment is released over a deposit zone. The dilution of the discharged material with seawater results in a variable solid volume fraction. The concentration of the sediment cloud appearing at the time of release is greater than 350 g/L and has an impact on the environment. Three different steps can be observed in this phenomenon: after the release, during the settling stage, sediments settle under a cloud of very high concentration; a second step is the material impact on the bed; the impact is followed by the formation of a turbidity current. Villaret [1] and Boutin [2] performed experiments of the release of sediment in a flume with and without currents. They were used as reference by Guillou et al. [3] to study the release and the formation of the density current by applying a two-phase flow model (NSMP-code). The choice of this kind of modeling is due to the high concentration of the mixture. Nguyen et al. [4] performed complementary simulations with the same code for two sand diameters and several lateral currents. Fluid flows are largely characterized by the coexistence of multiscale coherent structures revealing their

own spatial and temporal scales. Their identification is an essential step in the study of the physical processes involved in numerical or experimental data. Many analysis methods have been developed to examine the dynamics of these coherent structures (wavelets method, Lyapunov exponent, Q-criterion, or λ2-criterion). In this way, proper orthogonal decomposition (POD) is a commonly used method of data analysis. POD is a technique which allows the identification of the most energetic structures that contribute in a physical spatio-temporal set of realizations [5]. Thus, POD leads to the extraction of their dominant characteristic features: it is based on a spatial-dependent orthonormal basis and time-dependent orthogonal time functions. It can be used for the reconstruction of the most probable realizations (cf. Holmes et al. [6]). The snapshot POD technique [5] is well adapted to extract information from numerical data. Cizmas et al. [7] used it to extract the spatio-temporal pattern in fluidized beds and then to build a reduced order model of the gas and the interaction of solid particles. Other works have dealt with bubbles in multiphase flow [8–13] and used POD technique to obtain a model simulation of variable density flow and solute transport in the case of submarine groundwater discharge. The reduced model associated with Galerkin projections is able to reproduce and predict the model results with accuracy with less computational time. Model reduction for groundwater flow models has also been implemented by Vermeulen et al. [14] and Vermeulen et al. [15]. As previously observed, POD has been used in two-phase applications. In particular, some authors [16–20] have applied this specific technique to identify the dominant structures in the flow dynamics of horizontal slug flow commonly observed in many industrial processes. Both phases, the liquid (water or oil) and the gaseous, have been explored.

The study of the concentrated sediment release from the experimental results is limited to the characterization of the evolution of the turbidity distribution at falling time and sediment release. The measurement of the dynamics of both phases present in this complex phenomenon is not accessible with experimental techniques. This work deals with the high "concentrated" sediment release phenomena resulting from a two-phase solid-fluid numerical simulation. Moreover, the effect of the lateral ambient current is also studied. The snapshot POD technique can be applied on variables characterizing the solid fraction that cannot be easily obtained by the experimental way. The snapshot proper orthogonal decomposition one-component (1C) method was applied to the water–sediment mixture release phenomenon in a previous work (cf. Nguyen et al. [21]). The dominant features in space and time were extracted from the spatio-temporal dynamics of the simulations. Now, one scalar component and two vectorial component proper orthogonal decomposition have been applied, respectively, to the fluctuating solid phase volume fraction and solid phase velocities. More specifically, we focused on the contribution of the proper orthogonal decomposition two-component (2C) method applied on the solid phase velocities to improve the comprehension of the link between the dynamics of the solid phase and the dispersion of the particle dispersion. Moreover, this work could also be a preliminary step to propose, at a future time, a reduced order model for engineering application, concerning the falling process or the density current phase.

In the Section 2, the following are introduced: the sediment release experiment, the numerical modeling configuration, and the basis of the proper orthogonal decomposition technique. The Section 3 deals with the results obtained by POD for a water–sediment mixture release, with or without ambient current. The impact of the particle diameter is studied without an ambient current for two different kinds of sand; then, the impact of the ambient current is only examined for the smallest diameter case. Particular attention is paid to the analysis of the link between the dynamics of the solid phase volume fraction and velocities. Finally, conclusions are given in the Section 4.

2. Materials and Methods

2.1. Experimental and Modeling Configuration

2.1.1. Governing Equations and Configurations Studied

There are several modeling strategies to simulate the coupling between a fluid and solid from the two-phase discrete element method in which the motion of each particle is modeled to the general sediment transport model in an environment for which sediments have no influence on the fluid flow. Between them, there exists the Eulerian–Eulerian two-phase model for which a concentration of particle is considered. It allows us to better model the interaction between the water and the particles without simulating the motion of each particle [22]. After considering the particles' size and the size of the domain, we choose to use the two-phase Euler–Euler approach. The two-phase flow model used here is based on the Eulerian–Eulerian description of the sediment and water motion [4]. We used an in-house 2D-solver first developed by Barbry et al. [23] and improved substantially by Chauchat and Guillou [24] and Nguyen et al. [25]. It is based on the resolution of the two-phase Euler–Euler equation for fluids and particles using the finite difference method. It is based on the governing Equation (1), as follows, where the subscript k is "f" for fluid and "s" for solid phase:

$$\begin{cases} \frac{\partial(\alpha_k)}{\partial t} + \vec{\nabla}.\left(\alpha_k.\vec{u}_k\right) = 0 \\ \frac{\partial\left(\alpha_k.\vec{u}_k\right)}{\partial t} + \vec{\nabla}.\left(\alpha_k\vec{u}_k \otimes \vec{u}_k\right) = \frac{1}{\rho_k}\vec{\nabla}.\left(\alpha_k\left(-p_k\ \overline{\overline{I}} + \overline{\overline{\tau_k}}\right)\right) + \alpha_k.\ \vec{g} + \frac{1}{\rho_k}.\vec{M}_k \end{cases} \quad (1)$$

where α_k, $\vec{u}_k$, and ρ_k stand for the volume fraction, velocity, and density of phase k, respectively, $\vec{g}$ is the acceleration of gravity, $\vec{M}_k$ the inter-phase momentum transfer, p_k the pressure of phase k, and $\overline{\overline{\tau_k}}$ is the viscous term. The sum of volume fractions, α_k, is obviously equal to 1. $\alpha_k\ \overline{\overline{\tau_k}}$ is linked to shear rate tensors of each phase, $\overline{\overline{D_s}}$ and $\overline{\overline{D_f}}$ by the following Equation (2) [26]:

$$\alpha_f\ \overline{\overline{\tau_f}} = \mu_{fs}\overline{\overline{D_s}} + \mu_{ff}\overline{\overline{D_f}} \qquad \alpha_s\ \overline{\overline{\tau_s}} = \mu_{ss}\overline{\overline{D_s}} + \mu_{sf}\overline{\overline{D_f}} \quad (2)$$

The viscous coefficients are provided by Equation (3), in which the amplification factor β is provided by the model (Equation (4)) proposed by Graham [27] in the function of the inter-particle distance *dip* (Equation (5)). In that relation, d is the particle diameter and $\alpha_{s,max}$ is the maximum close packing concentration (close to 0.635 for non-cohesive spherical solid particles). Equations (3)–(5) are as follows:

$$\mu_{ff} = \alpha_f\mu_f, \quad \mu_{ff} = \alpha_f\mu_f, \quad \mu_{ss} = \alpha_s\beta\mu_{fs}, \quad \mu_{fs} = \alpha_s\mu_f \quad (3)$$

$$\beta = \frac{5}{2} + \frac{9}{4}\left(\frac{1}{1+\frac{dip}{d}}\right)\left[\frac{1}{\frac{2dip}{d}} - \frac{1}{\frac{1+2dip}{d}} - \frac{1}{\left(\frac{1+2dip}{d}\right)^2}\right]\frac{1}{\alpha_s} \quad (4)$$

$$\frac{dip}{d} = \frac{1-\left(\frac{\alpha_s}{\alpha_{smax}}\right)^{\frac{1}{3}}}{\left(\frac{\alpha_s}{\alpha_{smax}}\right)^{\frac{1}{3}}} \quad (5)$$

Moreover, the phase particle also plays a different role following the phase. The reader is referred to [4] for more information on the model, as it is not the main objective of this paper.

2.1.2. The Release Phenomenon

A recipient (maximum capacity of 60 L) containing a highly concentrated mixture of sand and water is placed at 15 cm below the free-water surface in a straight channel of 72 m long, of 1.5 m wide, and of 1.5 m height (Villaret [1] and Boutin [2]) with a current.

The measurement of the release (a camera that takes pictures every 0.5 s, and concentration measurements are obtained by using optical transducers placed at three fixed points) starts when the bottom of the recipient is opened (cf. Figure 1). After the release, two counter-rotating vortices [1] fall until the bottom have been observed. Then, a second phase appears in which the sediment cloud is expanding in the two lateral directions.

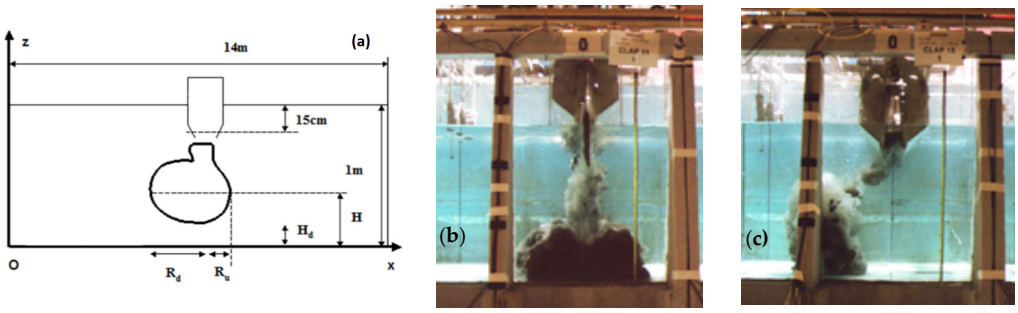

Figure 1. Illustrative sketch of the release phenomenon: (**a**) description of the sediment release experiments, Rd and Ru are, respectively, downstream and upstream radius of the sediment cloud front; (**b**) water–sediment mixture dumping without ambient current (D_{p1}); (**c**) water–sediment mixture dumping with ambient current (D_{p1}-U_{c20}).

Pure-sand experiments were performed for several parameters, namely the sediment diameters (D_p), the sediment release volumes (V_d), the initial concentrations of the mixture (C_m), and the imposed ambient current (U_c). Villaret [1] and Boutin [2] determined the falling time (time lapse between the release and the impact of the sediment cloud on the bottom), the up- and downstream radius of the cloud, the maximum height of the density current, and the front velocity of the density current (Table 1).

Table 1. Testing conditions of the simulated cases and nomenclature: T_f is the falling time defined from simulations, *Ns* is the size of the complete collection of snapshots outputted from simulation for each configuration studied, M the number of snapshots used in the POD decomposition ($\leq Ns$), W_{inj} is the injection velocity from the recipient, D_p the sediment particle diameter (90 µm or 160 µm), µ the dry density of the solid (2650 kg/m^3), Cm is the concentration of the mixture (450 g/L), V_r is the volume of dumped material (60 L), and U_c the ambient velocity [2].

Cases	D_{p1}	D_{p1} -U_{c10}	D_{p1} -U_{c20}	D_{p1} -U_{c15}	D_{p1}-U_{c25}	D_{p2}
Ns	200	200	159	183	140	400
T_f (s)	1.5	2.1	2.6	2.4	2.8	1.3
W_{inj} (m/s)	0.79	0.79	0.79	0.79	0.79	0.89
D_p (µm)	90	90	90	90	90	160
V_r (L)	60	60	60	60	60	60
U_c (cm/s)	0	10	20	15	25	0
Size of the decomposed collection	M = 15–200 (dt = 0.1 s)	M = 200 (dt = 0.1 s)	M = 159 (dt = 0.1 s)	M = 183 (dt = 0.1 s)	M = 140 (dt = 0.1 s)	M = 15–400 (dt = 0.1 s)

Moreover, both authors noticed that the experiment had a 2D development of the plume, in spite of the fact that the experimental domain had a square section. Thus, the 2D-solver previously presented was applied to obtain the numerical experiment.

2.1.3. Design of Numerical Experiments

The 2-D X/Z computation domain has a length of 14 m in the horizontal direction (positive upstream, centered to the dumping location) and over 1 m on the vertical one. A no-slip condition is fixed on the bottom and a slip condition is fixed at the top boundary. At the channel inlet, the fluid velocity is imposed, and no sediment is introduced. According to the recommendations of Nguyen [4] the opening of the recipient (width = 10 cm), the concentration and a Poiseuille parabolic profile of maximum velocity (W_{inj}) are imposed, assuring the right mixture discharge. Indeed, it was observed in this previous work that the Poiseuille-type profile is well suited to the experimental conditions. The values of the channel inlet velocity and the release are shown in Table 1. Two sand diameters are considered, namely D_{p1} = 90 µm (sand 1) and D_{p2} = 160 µm (sand 2). A uniform mesh of 1401 nodes on the horizontal and 61 vertical nodes were used, and the time step was fixed to 0.001 s. Data analyses were performed over the simulation outputs for every 0.1 s. This work is focused on the averaged motion, and the outputs timestep seems to be adapted to this characterization. It will serve for the POD analysis hereafter.

Cases D_{p1} (sand 1) and D_{p2} (sand 2), assumed in this work as reference cases, were previously presented by Guillou et al. [3]. They studied the evolution of the sediment cloud as well as solid velocity fields in still water for both cases. It was found that the two-phase model reproduces two counter-rotating vortices, as observed experimentally by Villaret [1] and Boutin [2].

Other simulations were performed in the case of release with a lateral ambient current in the channel for a given type of sand. As noticed by Nguyen et al. [4], these numerical results are in correct agreement with the experimental data. Indeed, as observed in Figure 2, for D_{p1} and D_{p2}, three steps are observed during a sediment release: the convective descent of the sediment cloud, the sediment cloud impact on the bottom, and the propagation of density currents up- and downstream until the equilibrium under the ambient current influence. For results obtained within an ambient current, only cases simulated for the sediment particle diameter of 90 µm and the ambient current going from 10 to 25 [cm/s] (D_{p1}-U_{c10}, D_{p1}-U_{c15}, D_{p1}-U_{c20} and D_{p1}-U_{c25}) will be studied.

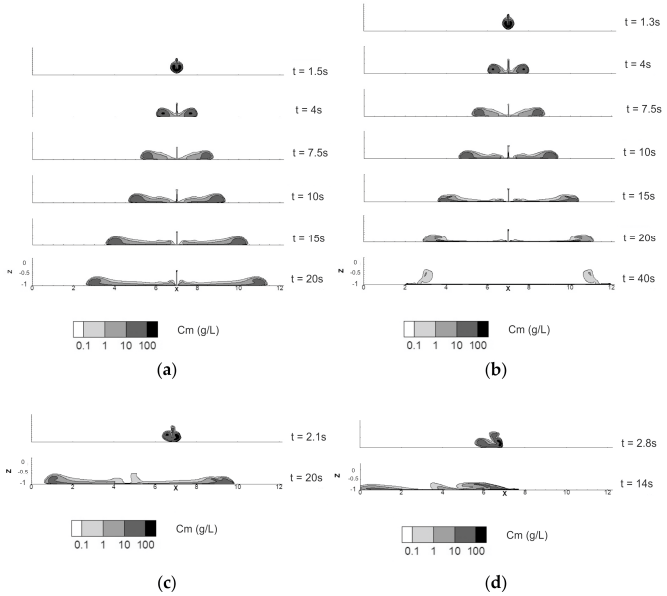

Figure 2. Instantaneous turbidity C_m [g/L] fields' evolutions obtained by simulations: (**a**) case D_{p1}; (**b**) case D_{p2}; (**c**) case D_{p1}-U_{c10}; (**d**) D_{p1}-U_{c25}. N represents the number of the snapshot. The first image of each case represents the turbidity distribution at falling time. In the cases without velocity (D_{p1}, D_{p2}), the sediments settle and move on the bottom in both directions until the total sedimentation of the particles, whereas in the cases with a current (D_{p1}-U_{c10}, D_{p1}-U_{c25}), the sediment plume is transported in the left direction until the limit of the simulation domain.

2.2. Proper Orthogonal Decomposition

2.2.1. Theoretical Aspects

POD is a powerful technique as it allows the identification of the energetic dominant spatial and temporal modes present in the flow. In this work, we will consider a set of M scalar or vectorial realizations represented by $u\left(\vec{x}, t_i\right)$, $i = 1,\ldots, M$; t_i represents the parameter time and $\vec{x}$ the position. POD extracts the orthonormal basis $\left\{\Phi_k\left(\vec{x}\right)\right\}$ of scalar or vectorial eigenfunctions, which maximizes the projection of the functions $u\left(\vec{x}, t_i\right)$ in a mean square sense.

Thus, to solve the POD problem it is necessary to define the average correlation function based on the inner product (.,.) and <.>, the ensemble average. $\|.\|$ is the norm, as follows:

$$R\left(\vec{x}, \vec{y}\right) = \left\langle u\left(\vec{x}, t_i\right) u^*\left(\vec{y}, t_i\right)\right\rangle \tag{6}$$

To obtain the solutions of the following eigenvalue (λ) problem, the following Equation (7) is used:

$$\int_D R\left(\vec{x}, \vec{y}\right)\Phi\left(\vec{y}\right)dy = \lambda\Phi\left(\vec{x}\right) \tag{7}$$

To identify $\left\{\Phi_k\left(\vec{x}\right)\right\}$ is equivalent to solving an optimization problem, i.e., the following Equation (8):

$$\frac{max\left\langle (u, \Phi)^2\right\rangle}{\|\Phi\|^2} \tag{8}$$

Every field realization can be written as the basis of the flow, as in the following Equation (9):

$$u\left(\vec{x}, t_i\right) = \sum_{k=1}^{\infty} a_k(t_i)\Phi_k\left(\vec{x}\right) \tag{9}$$

where a_k are the temporal orthogonal coefficients obtained from the projection of $u\left(\vec{x}, t_i\right)$ onto the $\left\{\Phi_k\left(\vec{x}\right)\right\}$ POD basis, as in the following Equation (10):

$$a_k(t_i) = \left(u\left(\vec{x}, t_i\right), \Phi_k\left(\vec{x}\right)\right),\ i = 1,\ \ldots,\ M \tag{10}$$

Due to the optimality of convergence in the energy of the POD basis, the realization can be projected onto the $\left\{\Phi_k\left(\vec{x}\right)\right\}$ POD basis and can be reconstructed as following from a small number (k_{max}) of spatio-temporal modes, as in the following Equation (11):

$$\widetilde{u}\left(\vec{x}, t_i\right) = \sum_{k=1}^{k_{max}} a_k(t_i)\Phi_k\left(\vec{x}\right), \quad i = 1,\ \ldots, M \tag{11}$$

An important property of the proper orthogonal decomposition is that temporal coefficients and eigenfunctions are uncorrelated in time and space. Thus, it is important to check that the following Equation (12) is correct:

$$\Phi_k^t\left(\vec{x}\right)\Phi_j\left(\vec{x}\right) = \delta_{jk} \tag{12}$$

$$\left\langle a_k^t(t).a_j(t)\right\rangle = \lambda_j\delta_{jk} \tag{13}$$

where δ_{jk} represents the Kronecker delta function.

More information about the basis of the POD properties is available in Holmes et al. [6].

According to the characteristics of the data decomposed by POD, the ensemble average differs, and it can be a spatial or a temporal one. The first one is used for data within a long-term history and moderate spatial resolution. For numerical simulation cases, as in

this work, the snapshot POD approach applies an ensemble average over the number of the realizations because it is efficient when the data have a high spatial resolution but a moderate-term history. For more information on the computational implementation of the snapshot POD, see Cizmas et al. [7].

In this paper, the focus is on solid volume fraction and solid phase velocity fields obtained from the numerical experiments (c.f. Section 2.1.1). In practice, one must first compute the time average $\overline{u}\left(\vec{x}\right) = \frac{1}{M}\sum_{i=1}^{M} u\left(\vec{x}, t_i\right)$ in order to construct a new velocity field with a zero average.

$\overline{\alpha}\left(\vec{x}\right)$ [-] is the mean field obtained from $\alpha\left(\vec{x}, t_i\right)$, the solid volume fraction fields snapshot collection, and $\vec{u}\left(\vec{x}\right)$ [m/s] is the mean field obtained from $\vec{u}\left(\vec{x}, t_j\right)$, the solid phase velocity fields snapshot collection selected to be decomposed. In this work, POD decomposition has been applied onto the difference between the mean fields. In the first case, a discrete version of the POD, POD_{1C}, will be applied onto the solid volume fraction fields snapshot collection, with $\alpha'\left(\vec{x}, t_i\right) = \alpha\left(\vec{x}, t_i\right) - \overline{\alpha}\left(\vec{x}\right)$. In the second case, two component vectorial POD_{2C} will be applied onto fluctuating solid phase velocity fields $\vec{u'}\left(\vec{x}, t_j\right) = \vec{u}\left(\vec{x}, t_j\right) - \vec{u}\left(\vec{x}\right)$, and this leads to spatial eigenfunctions within two-component vectors. To represent these eigenfunctions, it is necessary to calculate a pseudo-vector field equal to the rotational of the two-component vectors field. The choice of the size M of the snapshots collection decomposed by POD technique (cf. Table 1) will be discussed in the following.

For POD decompositions, a small number of spatio-temporal modes are necessary to perform an optimal reconstruction of the realizations in the energy sense. Each eigenvalue corresponds to the information carried by each eigenmode; in other words, it corresponds to its energy contribution. The total POD energy captured in a decomposition of a data set is equal to the sum of all POD eigenvalues λ_j. Thus, for POD_{1C} and POD_{2C}, we, respectively, obtain $E(\alpha'_s)$ [ ] and $E(u'_s, w'_s)$ [m^2/s^2]. The average root mean square error percentage highlights the relative difference between an original set of realizations and a reconstructed one.

2.2.2. About the Size of the Snapshot Collection Decomposed by POD

POD decomposition can be applied to different collections of snapshots selected from the total snapshot sequence output from the numerical simulations. For D_{p2}, dt is 0.1 s and Ns = 400 (total time = 40 s). The size of the sequence decomposed, with dt = 0.1 s, has been selected equal to M = 40 (short collection with a total time of 4 s) and M = 400 (long collection). Considering dt = 0.2 s, new snapshot collections can be extracted from the initial one and, thus, M is, respectively, equal to 20 (4 s) and 200 (40 s).

Figure 3 shows the average root mean square error between the original simulation realizations and the reconstructed fields for a short duration time of 4 s (a) and a longer one of 40 s (b) (k_{max} is the number of POD spatio-temporal modes used in the reconstruction). In both cases, for a fixed total time sequence, no significant differences are observed in spite of the change in the sampling frequency. Both decompositions, based on (α'_s) and (u'_s, w'_s), lead to a similar accuracy of reconstruction for a given k_{max} (cf. Figure 3). The average root mean square error obviously decreases with the increase in k_{max}. Note that it can be observed that, for a given k_{max}, the average root mean square error is lower for the POD decomposition based on (u'_s, w'_s). These results verify that the good choice of the snapshot collection decomposed by POD is not strictly linked to the snapshot dt. The POD results presented in the following have been obtained from snapshot sequences computed with dt = 0.1 s, which seems to be sufficient to lead to suitable decomposition with a short or a long sequence of realizations. The parameters (M, dt) are defined according to the steps of the release phenomenon that will be studied.

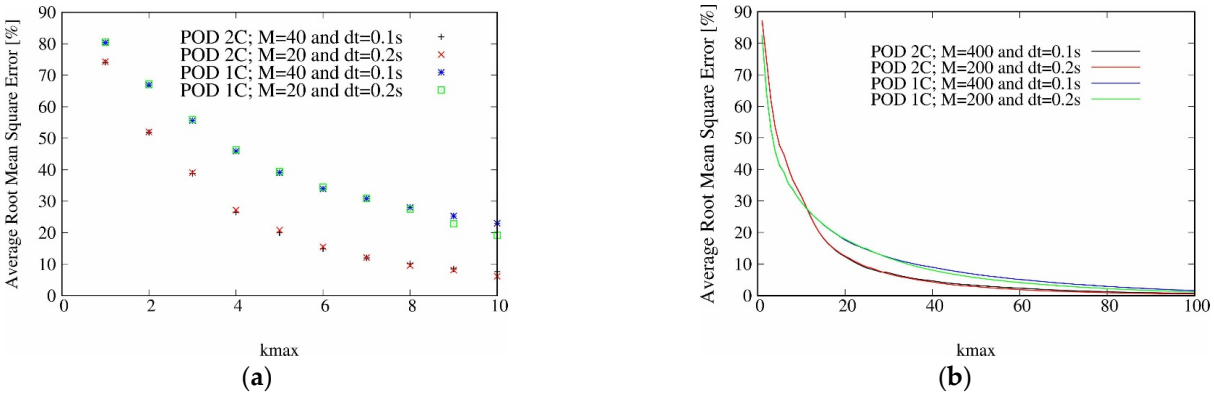

Figure 3. Average root mean square error percentage according to k_{max}, the number of POD spatio-temporal modes used in the snapshot reconstruction. The duration time of a sequence is equal to 0.1 *M*. The results shown in this figure are extracted by POD_{1C} and POD_{2C} for D_{p2} particles applied to snapshot collections with a short duration time of 4 s (**a**) and a longer one of 40 s (**b**).

3. POD Results for a Water–Sediment Mixture Release

In the following, a one-component scalar decomposition POD_{1C} is applied to the fluctuating solid volume fraction fields and a two-component vectorial decomposition POD_{2C} is applied to the fluctuating solid phase velocities fields. Reference cases D_{p1} (for D_p = 90 µm) and D_{p2} (for D_p = 160 µm), respectively, present water–sediment mixture release without ambient current configurations. POD decompositions are performed on different sized snapshot collections for case D_{p1} (M = 15; 40; 75; 100; 150; 200, and a total sequence time going from 1.5 s to 20 s) and D_{p2} (M = 13; 40; 75; 100; 150; 200; 250; 300; 350; 400, and a total sequence time going from 1.3 s to 40 s).

As previously noticed by Nguyen et al. [4], until a time of 20 s, the three steps of the release phenomenon are identified (cf. Figure 2) in the numerical results: the convective descent during which the sediment falls under the influence of gravity, the collapse occurring when the descending cloud or jet impacts the bottom dispersion, and the passive transport beginning with the sediment transport and its spreading.

Because of release are studied in a quiescent water, sediment transport is quickly stopped and, thus, sediment spreading occupation zone is limited in the domain. As noticed by Nguyen et al. [4], in both cases, the propagation is symmetric and linear for a short time, and the position of the front of the density current reaches nearly 4 m at a time equal to 20 s. As such, choosing M = 200 (20 s) as size of the snapshot collection (in D_{p1} and D_{p2} cases) to apply POD decomposition and to compare the results extracted seems suitable (for the release phenomenon going on until the sediment transport).

The convective descent of the sediment cloud is characterized by a falling time (T_f). Two different processes are involved in this phenomenon: on the one hand the density effect of the sediment–water mixture, like a saline water plume, and, in the other hand, the terminal settling velocity of individual particles. The time required for the plume to reach the bottom depends on both processes. Table 2 shows T_f obtained by Villaret [1] and Boutin [2], the results obtained in the present work, and by Farout-Fréson [28]. Note that Farout-Fréson [28] proposed a model based on the averaged form of the hydrodynamic biphasic equations, coupled to a sediment transport equation with a specific numerical settling velocity. This model was calibrated on the experimental campaigns of Villaret [1] and Boutin [2].

Table 2. Sediment cloud falling time (T_f) obtained for a mixture concentration of 450 g/L.

	Falling Time for the Case D_{p1}	**Falling Time for the Case D_{p2}**
Experimental results (Villaret [1] and Boutin [2])	0.95 (0.45–1.45)	0.72 (0.22–1.22)
Numerical results in this work	1.5	1.3
Numerical results—bi esp2D (Farout-Fréson [28])	1	0.7

Note that, in an opposite way to the numerical results presented in here, the Villaret [1] and Boutin [2] experimental results were obtained without a control of the injection velocity profile. In the present work, in both cases, D_{p1} and D_{p2}, convective descent of the sediment cloud is characterized by a falling time (T_f) of 1.5 s and 1.3 s (cf. Table 2) observed in the instantaneous field series. The experimental fall time was extracted from snapshots taken of the generated turbid plume with a synchronized camera. This implies an important uncertainty of 0.5 s. Thus, numerical results presented in this paper can be considered as satisfactory despite being superior to that of the upper limit observed for experimental results. It can be seen that the reduction in the falling time due to a greater D_p turns out to be slight.

3.1. POD of Snapshots Collections Describing Falling Time

For the first time, we focused our analysis on POD decompositions obtained for snapshot collection limited to the convective sediment cloud descent. Thus, $M{\sim}T_f/0.1$ was chosen as equal to 15 for D_{p1} (which corresponds to time T_f = 1.5 s) and 13 for D_{p2} (T_f = 1.3 s).

Figure 4a (i.e., Figure 4b) shows the mean solid volume fraction field (i.e., mean solid phase velocity field) for D_{p1} and POD_{1C} (i.e., for D_{p1} and POD_{2C}) and also the first spatial eigenfunctions extracted from the difference compared to the mean field, in other words the eigenfunctions linked to the most energetic eigenvalues.

The spatial dimensionless eigenfunctions extracted by POD_{2C} (cf. Figure 4b) present strong and compact couples of counter-rotating structures or POD modes associated to the appearance and growing of symmetrical vortices during the falling of the water–sediment mixture. The number of the POD modes observed in an eigenfunction $\Phi_k\left(\vec{x}\right)$ increases with the index k. Similarly, the eigenfunctions obtained from the POD_{1C} decompositions exhibit aligned and piled POD modes (cf. Figure 4a). This arrangement is, obviously, strictly associated to the convective descent of sediment. The eigenfunctions extracted for the D_{p2} case are not shown here. The spatio-temporal modes extracted from this snapshot collections have broadly similar characteristics to the D_{p1} case. However, the increase in D_p, leading to the enhancement of the particles' weight, implies the elongation in the form of the POD modes.

As observed in Figure 4c (i.e., Figure 4d), the four first $a_i(t)$ temporal coefficients extracted from the decomposition POD1C of the difference compared to the mean solid volume fraction (α_s')(i.e., POD2C of the difference compared to the mean solid volume velocities (u_s', w_s')) show oscillations. For $a_3(t)$ and $a_4(t)$, the oscillations are twice as short as for $a_1(t)$ and $a_2(t)$. The phase space projections $(a_1(t), a_2(t))$ and $(a_3(t), a_4(t))$ illustrate the correlation between the temporal coefficients of the most energetical eigenfunctions and their relative frequency (cf. Figure 4e,f) (the two first eigenvalues have an energy contribution greater than 20% and for the two next ones, the individual contribution is lower than 10%. The choice was, therefore, made to verify the phasing of the dynamics between eigenmodes whose energy contributions are of the same order). The harmonious shape of curves indicates a strong correlation between the two temporal coefficients shown in the projection. For the POD_{1C} applied to a snapshot collection corresponding to the

falling time, $(a_1(t), a_2(t))$ has a circular shape, while $(a_3(t), a_4(t))$ seems to have a temporal pattern close to $T_f/2$.

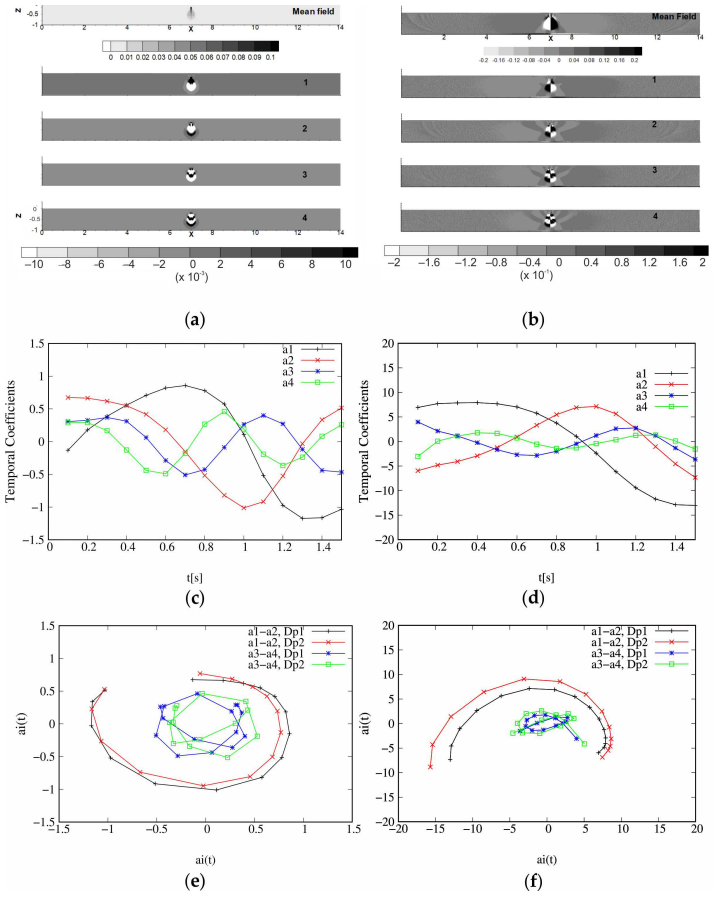

Figure 4. Results obtained for the D_{p1} case for POD applied to a snapshot collection corresponding to the falling time T_f = 1.5 s (dt = 0.1 s and M = 15). (**a**) Mean solid volume fraction field and POD_{1C} spatial dimensionless eigenfunctions $\Phi_k\left(\vec{x}\right)$ obtained from the difference compared to the mean solid volume fraction (α_s') ; (**b**) mean solid phase velocity field and POD_{2C} spatial dimensionless eigenfunctions $\Phi_k\left(\vec{x}\right)$ obtained from the difference compared to the mean solid volume velocities (u_s', w_s'). Dark colours represent positive values and clear colors represent negative values; (**c**) POD_{1C} temporal orthogonal coefficients $a_j(t)$ (**d**) POD_{2C} temporal orthogonal coefficients $a_j(t)$; (**e**) phase space projections of temporal coefficients obtained through the POD_{1C} for D_{p1} and D_{p2} cases; (**f**) phase space projections of temporal coefficients obtained through the POD_{2C} for D_{p1} and D_{p2} cases.

Note that in the POD_{2C} case, the characteristic time of the phase space projections $(a_1(t), a_2(t))$ seem to be a slightly longer that in the POD_{1C} case. It can be inferred that the dynamics of the phenomenon have a small difference for the solid volume fraction and the solid volume velocities behaviors.

Moreover, these phase space projections reveal a similar phasing during the falling time, despite the modification of the sediment particle diameter. In other words, the dynamics of the most energetics eigenfunctions extracted from the difference compared to the mean solid volume fraction and the difference compared to the mean solid volume velocities stay unchanged.

From the energetic point of view, it can be observed that (cf. Table 3), as expected, the total kinetic energy values $E(u_s', w_s')$ and $E(u_s', w_s')$ are mainly accumulated in the first eigenvalue. The contribution $\lambda_1 / E(u_s', w_s')$ is close to ~65%, and $\lambda_1 / E(\alpha_s')$ is close of ~42% for both POD_{1C} and POD_{2C}.

Table 3. Energy contribution of the modes for POD applied to snapshot collection limited to the falling time.

	D_{p1} M = 15 (1.5 s)	D_{p2} M = 13 (1.3 s)
$E(\alpha'_s)$	1.27	1.19
$E(u'_s, w'_s)$	98	140
$\lambda_1/E(\alpha'_s)[\%]$ and $\lambda_2/E(\alpha'_s)[\%]$	44, 28	42, 29
$\lambda_1/E(u'_s, w'_s)[\%]$ and $\lambda_2/E(u'_s, w'_s)[\%]$	68, 23	64, 24
$(\lambda_1+\lambda_2+\lambda_3)/E(\alpha'_s)[\%]$	80	79
$(\lambda_1+\lambda_2+\lambda_3)/E(u'_s, w'_s)[\%]$	96	94

Moreover, note that only three modes are necessary to reach more than 95% of the kinetic energy $E(u'_s,\ w'_s)$ and contain the dynamics of the difference compared to the mean solid volume fraction flow. The behaviour of the difference compared to the mean solid volume fraction seems to be more complex; indeed, more spatio-temporal modes are necessary to contain the same percentage of $E(\alpha'_s)$ equal to 80%.

D_p has an impact on the amount of total energy extracted (cf. Table 3). On the one hand (POD_{1C}), the D_p impact on the dynamics of the volume fraction is slight (a reduction of 7%), and on the other hand (POD_{2C}), its impact on the velocity field reaches 30% of augmentation. Moreover, note that the distribution of the contributions of the first four values remains, with very slight differences, the same for the two particle diameters. This confirms that the dynamics of these phenomena are weakly impacted by the modification of the diameter of the particles. Thus, the particle size and its weight seem to have a modest impact on the solid volume fraction distributions during the sediment descent stage; however, this impact is most marked on the level of agitation of the solid phase velocities.

3.2. POD for Snapshot Collection Describing All the Release Phenomenon

In the following, we will focus our analysis on decompositions obtained for snapshot collections with a size M growing from 15 (13) for the case D_{p1} (D_{p2}) until 200, with dt = 0.1 s; in other words, from a short duration of 1.5 s (1.3 s) to a duration of 20 s, describing the three steps of the release phenomenon. For D_{p2}, complementary decompositions have been made for values of M until from M = 400 (a duration of 40 s). Figure 5 shows the evolution of the total energy (E) captured by POD decompositions according to the number of snapshots M decomposed for α'_s and for (u'_s, w'_s) for D_{p1} and D_{p2}.

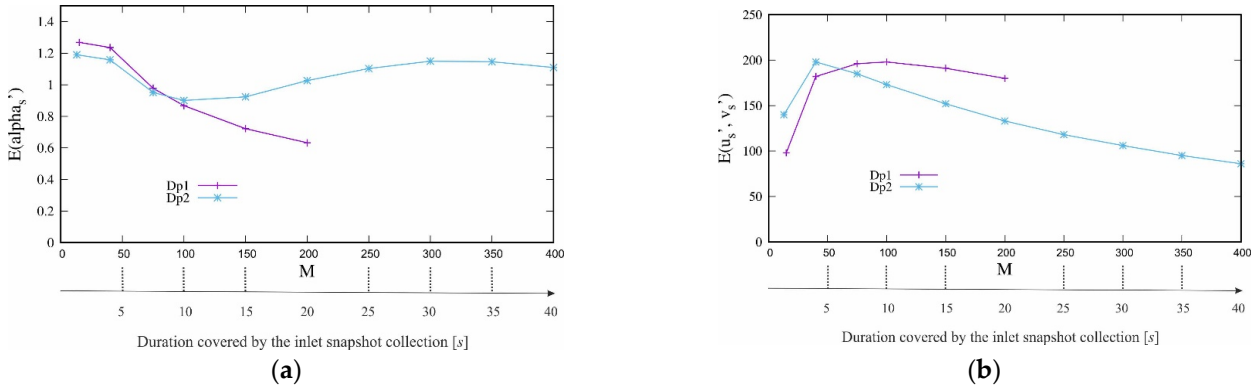

Figure 5. (**a**) Total POD_{1C} energy ($E(\alpha'_s)$ [ ]) and (**b**) total POD_{2C} energy ($E(u'_s,\ w'_s)$ [m^2/s^2]) according to the M number of snapshots decomposed for D_{p1} and D_{p2}. Here, dt is equal to 0.1 s, and the duration of the size collection is equal to Mdt.

The energetic aspect has been completed by information dealing with the spatial dimensionless eigenfunctions extracted by POD_{1C} and POD_{2C} applied on snapshot collections obtained for D_{p1} and M = 200 and a duration of 20 s (cf. Figures 6 and 7 for D_{p1}).

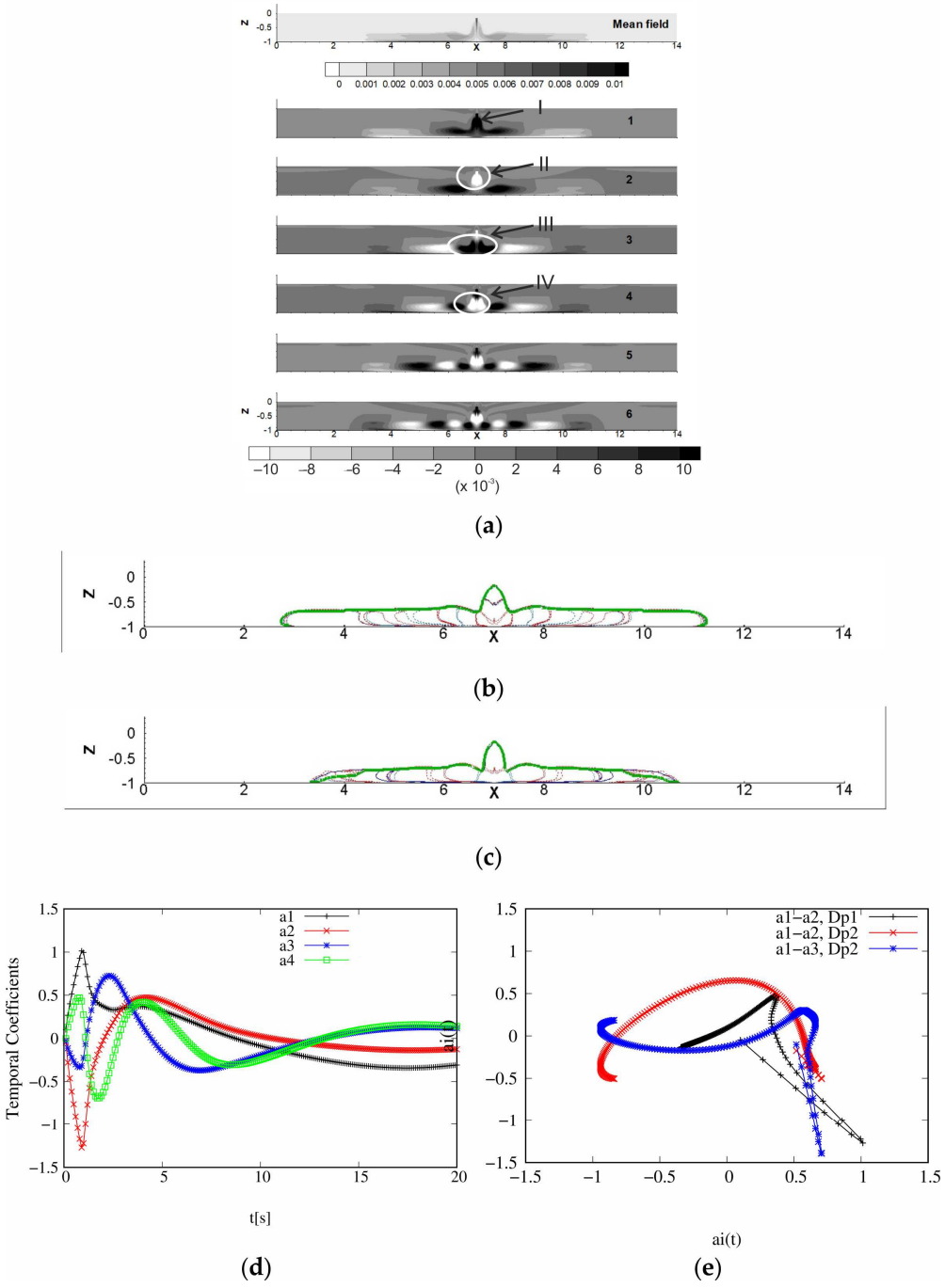

Figure 6. (**a**) Mean solid volume fraction field and POD_{1C} spatial dimensionless eigenfunctions $\Phi_k\left(\vec{x}\right)$ obtained from the D_{p1} case for the difference compared to the mean solid volume fraction (α_s') and M = 200 (dark colours represent positive values and clear colors represent negative values). (**b**) Particle's cloud outline (solid line) superimposed to the four first eigenfunctions for M = 200. (**c**) Particle's cloud outline (solid line) superimposed to the four first eigenfunctions for the D_{p2} case M = 200. (**d**) POD_{1C} temporal orthogonal coefficients $a_j(t)$. (**e**) Phase space projections of temporal coefficients obtained through the POD_{1C} for the D_{p1} and D_{p2} cases.

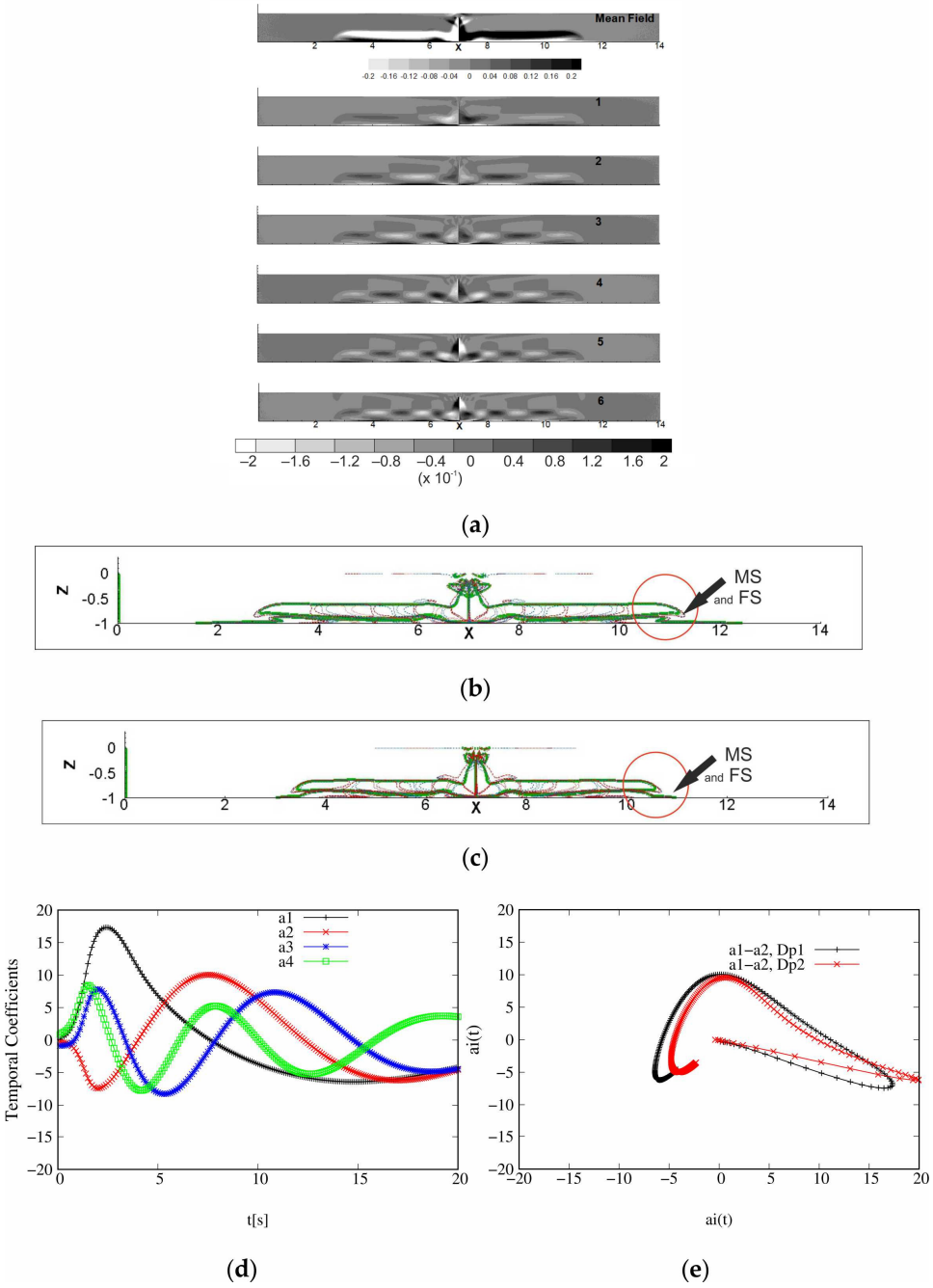

Figure 7. (**a**) Mean field and POD_{2C} spatial dimensionless eigenfunctions $\Phi_k\left(\vec{x}\right)$ obtained from the D_{p1} case for the difference compared to the mean solid volume velocities (u'_s, w'_s) and $M = 200$ (with POD_{2C} we obtain dimensionless spatial eigenfunctions; however, we have represented the rotational of each eigenfunction. Dark colors represent positive values and clear colors represent negative values). (**b**) Outline obtained for the solid volume fraction velocities (solid line) superimposed to the four first eigenfunctions for the D_{p1} case $M = 200$. (**c**) Outline obtained for the solid volume fraction velocities (solid line) superimposed to the four first eigenfunctions for the D_{p2} case $M = 200$. (**d**) POD_{2C} temporal orthogonal coefficients $a_j(t)$. (**e**) Phase space projections of temporal coefficients obtained through the POD_{2C} for D_{p1} and D_{p2} cases (as observed for the phase space projection $(a_1(t), a_2(t))$ (cf. Figure 7e), $(a_1(t), a_3(t))$ and $(a_2(t), a_3(t))$ also present similar shapes for both particle diameters. This finding suggests that, despite the differences observed elsewhere related to the impact of the diameter of the particles, the difference compared to the mean solid volume velocities maintain a similar dynamic).

The contribution of the three most energetic eigenvalues to the total energies $E(\alpha'_s)$ and $E(u'_s, w'_s)$ are presented in the Table 4. Note that, with the increase in the particle diameter, $(\lambda_1 + \lambda_2 + \lambda_3)/E(u'_s, w'_s)$ stays close to ~62%, while $(\lambda_1 + \lambda_2 + \lambda_3)/E(\alpha'_s)$ passes from 43% (for D_{p1}) to 63% (for D_{p2}). Thus, the particle's size and its weight seem to have an impact on the complexity of the behavior compared to the mean solid volume fraction.

Table 4. Energy contribution of the modes for POD applied to a snapshot collection describing the release phenomenon.

	D_{p1} M = 200 (20 s)	D_{p2} M = 200 (20 s)
$E(\alpha'_s)$	0.63	1.03
$E(u'_s, w'_s)$	180	133
$(\lambda_1 + \lambda_2 + \lambda_3)/E(\alpha'_s)$[%]	43	63
$(\lambda_1 + \lambda_2 + \lambda_3)/E(u'_s, w'_s)$[%]	62	64
Number of eigenvalues necessary to reach 95% of $E(\alpha'_s)$	15	18
Number of eigenvalues necessary to reach 95% of $E(u'_s, w'_s)$	10	10

In the same way as seen in the previous paragraph, for decompositions limited to the falling time snapshot collections, a small number of spatio-temporal modes is enough to extract 95% of the total energy. In the case relative to the solid volume fraction velocities, there were 10 modes (compared to the 200 modes extracted) in the POD_{2C} decomposition based on the parameter (u'_s, w'_s) and 15–18 in the POD_{1C} decomposition based on (α'_s). It is clear that, for this specific set-up, it would be possible to obtain a reduced-order model covering the different steps of the sediment release.

For POD_{2C} applied to (u'_s, w'_s) and the D_{p1} case, the total kinetic energy contained by the two initial counter-rotating vortices increases until a maximum value of 198 reached M = 100, corresponding to a total collection time of ~10 s (cf. Figure 5b). This growth observed during (and just beyond) beyond the falling time implies an enhancement in the level of agitation of the solid phase velocities linked to the sediment descent. For snapshot collections with a size $M > 100$, $E(u'_s, w'_s)$ slowly decreases with M values, to reach 180 at 20 s. This implies that the level of agitation of the flow during the entire event, and more particularly during the formation of a turbidity current, become weaker. It is be reasonable to associate it with the mixing and dilution of the sediment. Thus, it is not surprising to observe (cf. Figure 5a) for POD_{1C} applied to (α'_s) that the energy curve decreases for D_{p1} from 1.19 to 0.86 (for a duration of 10 s) and 0.63 (for 20 s).

What is the impact of D_p on the evolution of $E(u'_s, w'_s)$ according to the size (M) of the decomposed snapshot collection? Additional decompositions resulted in D_{p2} and M growing up to 400. Note that for $M > 200$ the snapshot collections contain a lot of data relative to the turbidity current step. The slight decrease observed for D_{p1} is most drastic and earliest for the largest particle diameter case D_{p2}: in this case $E(u'_s, w'_s)$ decreases from 198 (for a duration of 5 s) to 133 (for 20 s) and 86 (for 40 s). It seems that, as observed for the vertical descent phase of the release, the marked influence of the particle size and weight is also present during the passive transport of the sediment leading to a resistance opposed to the motion of the solid phase. In an opposite way, for the $E(\alpha'_s)$ curves (cf. Figure 6a) the trend observed for D_{p1} and D_{p2} becomes different at around M = 100. Indeed, while $E(\alpha'_s)$ continues to decrease for D_{p1}, for the largest particle diameter case D_{p2} we observe an augmentation until ~1.1 for 20 s, and then a stabilization until 40 s. This trend is observed for POD_{2C} applied to inlet snapshot collections including the third step of the release phenomenon, characterized by a long and complete collapse of sediment, concentrated at the bottom (cf. Figure 2b). Indeed, as observed by Nguyen et al. [5], the radius of the particle bed grows and reaches nearly 4 m for a total time of 20 s in both D_p cases. However, the collapsing of the sediment mixture differs until time $t > 15$ s.

Eigenfunctions extracted for the D_{p1} case for POD_{2C} applied on the difference compared to the mean solid volume velocities snapshots (cf. Figure 7a) reveal well-defined POD modes, which also support the existence of a low complexity of the dynamics. In the same way, the temporal coefficient reveals a marked temporal organization (cf. Figure 7d,e). The marked oscillations observed during the first seconds are smoothed after the falling time. The phase space projection $(a_1(t), a_2(t))$ present a harmonious shape. For D_{p1}, the footprint of falling and collapse of the water–sediment mixture is present on the four most energetic POD_{2C} eigenfunctions. They put to the fore strong counter-rotating structures associated to the appearance of the initial counter-rotating vortices due to sediment falling and water–sediment mixture collapse. All these eigenfunctions present POD modes stretched on the bottom. Indeed, the opposition of the quiet water to the motion implies their stretched shape. For $k \geq 3$ other compact, counter-rotating, and symmetrical POD modes of $\Phi_k\left(\vec{x}\right)$ evolve parallel to the bottom, above the flat POD modes previously described. Their size decreases with the increasing index.

Eigenfunction sets extracted within POD_{1C} also reveal well-defined compact and strong POD modes. Temporal coefficient also reveals a marked temporal organization (cf. Figure 6d,e) (as will be noticed in the following, for the snapshot collection describing all the release phenomenon, the contribution of the first eigenvalues is less marked than in the falling time snapshot collection case. The three, or even the first four, eigenvalues can have contributions of the same order. Also, drawing other curves $(a_1(t), a_3(t)), (a_1(t), a_4(t)), (a_{12}(t), a_3(t)), \ldots$ may be relevant. As can be observed (cf. Figure 6e), the phase space projection $(a_1(t), a_2(t))$ for the two particle diameters studied in this work have different shapes. However, it can be observed that there is a similarity between $(a_1(t), a_2(t))$—D_{p1} and $(a_1(t), a_3(t))$—D_{p2}.). Note that the oscillations fade faster to reach constant values, thus, the dynamics of the solid volume fraction seem to reach a stability ahead of the dynamics of the solid volume velocity. In the D_{p1} case (cf. Figure 6a), the two most energetic eigenfunctions, namely $\Phi_1\left(\vec{x}\right)$ and $\Phi_2\left(\vec{x}\right)$, show central POD modes (labelled I and II) strongly linked to the water–sediment mixture falling; they also present a symmetrical couple of modes dealing with the deposit of the water–sediment mixture after its collapse and the transport of the particle cloud. $\Phi_3\left(\vec{x}\right)$ seems to be also marked by collapse and the deposit of water–sediment mixture. POD modes labelled III and IV (cf. Figure 6a) are linked to the sediment collapse, while the other ones are linked to the density current. For D_{p1}, one layer of strong symmetrical POD modes on the bottom, linked to the progressive passive transport of density, appears for $\Phi_k\left(\vec{x}\right)$ with $k \geq 5$ and $k \geq 6$ for D_{p2}. In the case of D_{p1}, the POD modes have regular contours, while for D_{p2} they seem to be weaker and less regular. For D_{p2}, the presence of a larger particle diameter D_p implies that the POD modes (I and II) linked to the deposit of the water–sediment mixture are also present in the third eigenfunction.

To define the outline for the solid volume fraction velocities, we identified the places where there is no motion of the solid volume during all the mixture release. Figure 7b,c show outlines superimposed on the four first eigenfunctions, respectively, for D_{p1} and D_{p2}. The mean field presents two main counter-rotating and symmetrical structures (MS). The interaction with the surface leads to the appearance of flat structures (FS) along the bottom. The MS structure on the right turns in the clockwise sense (as observed in the mean solid volume fraction velocity field, cf. Figure 7a), inducing the mixing of the flow and, thus, a water–sediment mixture resuspension. The right flat structure (FS) turns in the anti-clockwise sense and induces the retention of the water–sediment mixture. All of the most energetic eigenfunctions present the two layers of POD modes previously identified. For D_{p1}, the main structures (MS) overcome and overtake the coherent creeping structures (FS) (cf. Figure 7b). As a result, the cloud outline does not show any crushing (cf. Figure 6b). Note that the particle cloud was identified as the place where the solid volume fraction becomes different to 0 during the mixture release. The cloud outline is the front of the particle cloud. In the opposite way, for D_{p2}, the lower layer extends almost as far as the

upper one (cf. Figure 6c) and the density front of the particle cloud outlines a crushing in its extremity. Thus, it is not surprising to observe the external POD modes collapsing due to the resistance of the bottom to transport of sediments (more difficult density transport). This slump is due to the slowdown in the front density observed in the turbidity snapshots (cf. Figure 2b). Thus, the influence of the size and the weight of the particles due to a larger D_p induces to POD modes more marked by the settling of the water–sediment mixture after the sediment collapse.

To retrieve the settling information by the way of the POD_{1C}, we associate the base parameter (α'_s) to the duration covered by the inlet snapshots collection, which needs to be sufficient to clearly observe the settling in the concentration field (cf. Figure 2). POD_{2C} is associated with the two-dimensional base parameter (u'_s, w'_s), and it presents the advantage of revealing the trends based on shorter snapshots collections than in the POD_{1C} because the inlet data contains the settling velocity data.

3.3. Impact of the Ambient Current

In the following section, the impact of the ambient current on the water–sediment mixture release for D_{p1} will be studied. POD_{1C} and POD_{2C} will be applied to determine the differences between the mean solid volume fraction fields and the mean solid phase velocities fields for cases within an ambient current going from U_c = 10 cm/s to U_c = 25 cm/s (D_{p1}-U_{c10}, D_{p1}-U_{c15}, D_{p1}-U_{c20}, D_{p1}-U_{c25}).

Figure 8 shows the impact of U_c on the total energy extracted by both decompositions applied in this work for sand 1. Figures 9 and 10, respectively, present eigenfunctions obtained from the (α'_s) and (u'_s, w'_s) snapshot decompositions for the cases D_{p1}-U_{c10} and D_{p1}-U_{c25}.

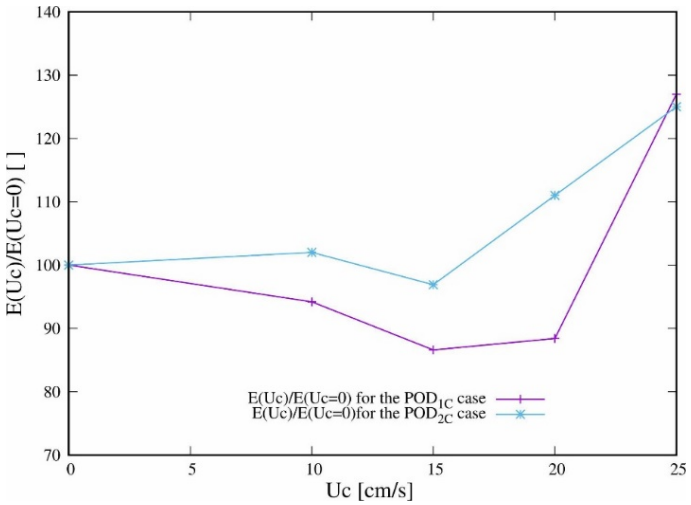

Figure 8. Total POD energy for sand 1 according to the ambient current: $E(\alpha'_s)$ [ ] extracted from solid volume fraction snapshots collection and total kinetic energy $E(u'_s, w'_s)$ [m^2/s^2]. Both values are dimensionless by the values obtained without an ambient current: 0.63 for POD_{1C} and 180 for POD_{2C}.

As noticed by Nguyen et al. [4], ambient current (Uc) breaks the symmetry of the turbidity distribution during the water–sediment mixture release (cf. Figure 2c,d). The water–sediment mixture occupation zone is shifted to the upstream direction. Thus, during 20 s after water–sediment mixture release, the downstream radius linearly increases from 4 m (for U_c = 0 cm/s) to 10 m for (U_c = 25 cm/s). The upstream radius linearly decreases from 4 m to nearly 0 because the propagation velocity of the front of the density current on the bottom decreases with U_c. Thus, for the cases with ambient velocity, the number of calculation steps (*Ns*) necessary to observe that the sediment cloud is out of the computation domain, but goes down with increasing ambient velocity (cf. Table 1). To analyze and

compare the water–sediment mixture release phenomenon, the size M of the collection of decomposed snapshots is chosen to be equal to Ns.

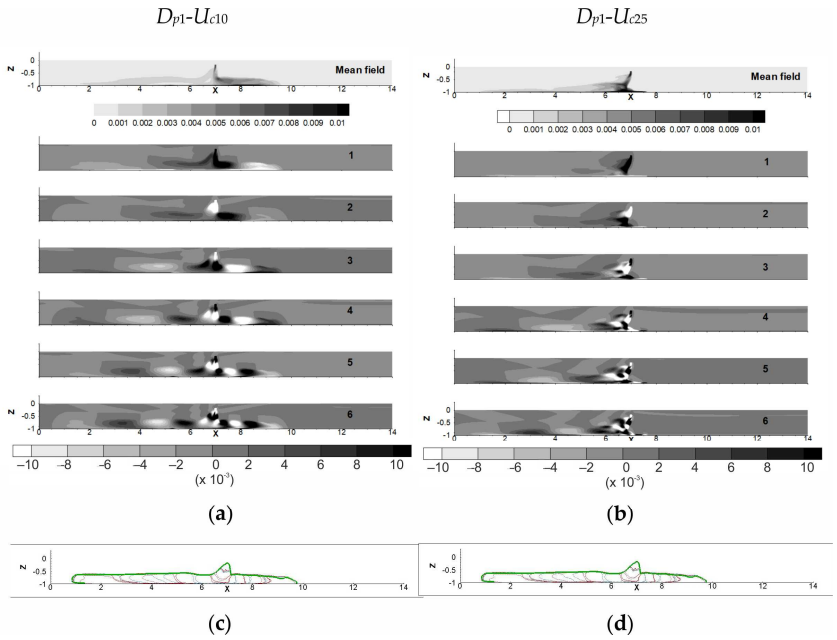

Figure 9. Mean solid volume fraction field and POD1C spatial dimensionless eigenfunctions $\Phi_k\left(\vec{x}\right)$ obtained for the difference compared to the mean solid volume fraction ($\alpha_s{}'$). Dark colors represent positive values and clear colors represent negative values: (**a**) D_{p1}-U_{c10} (M = 200); (**b**) D_{p1}-U_{c25} (M = 140); (**c**) particle's cloud outline (solid line) superimposed to the four first eigenfunctions for D_{p1}-U_{c10} and (**d**) for D_{p1}-U_{c25}.

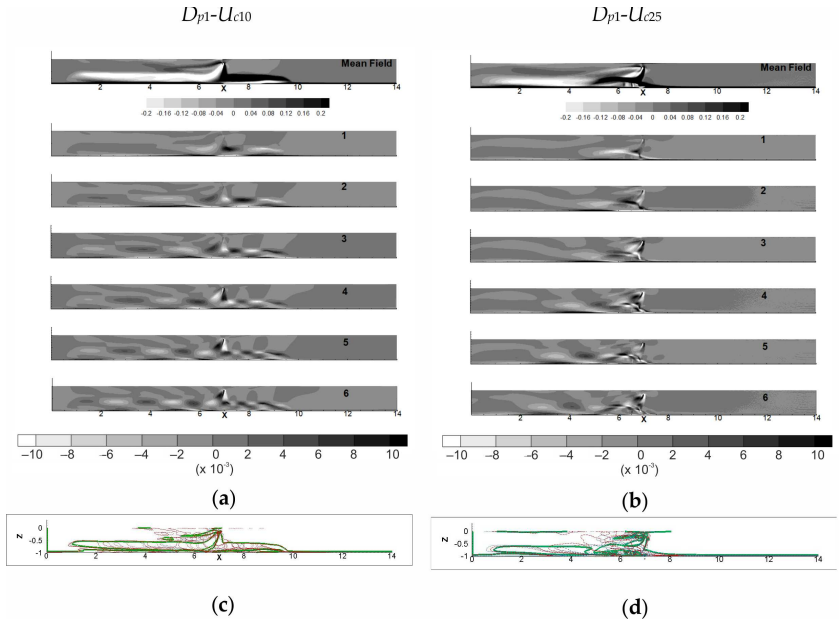

Figure 10. Mean solid phase velocity field and POD_{2C} spatial dimensionless eigenfunctions $\Phi_k\left(\vec{x}\right)$ obtained for the difference compared to the mean solid volume velocities (u_s', w_s'). To represent these eigenfunctions, it is necessary to calculate a pseudo-vector field equal to the rotation of the two-dimensional vector field. Dark colors represent positive values and clear colors represent negative values: (**a**) D_{p1}-U_{c10} (M = 200); (**b**) D_{p1}-U_{c25} (M = 140); outline obtained for the solid volume fraction velocities (solid line) superimposed to the four first eigenfunctions for (**c**) D_{p1}-U_{c10} and (**d**) for D_{p1}-U_{c25}.

$E(\alpha'_s)$ and $E(u'_s, w'_s)$ are presented in Table 5 for different values of U_c. As previously noticed, for U_c = 0 cm/s and POD_{2C} decomposition is based on the parameter (u'_s, w'_s) and 10 modes (compared to the M = 200 modes extracted), in other words 5% of M. This ratio evolves until it reaches 7.9% with the increasing U_c. The presence of the ambient current leads to a modest increment in the number of eigenvalues necessary to reach 95% of the total energy extracted. A similar trend is observed for results extracted by POD_{1C} (cf. Table 5).

Table 5. Energy contribution of the modes for POD applied to a snapshot collections describing the density current propagation for cases within current ambient.

	D_{p1} M = 200 (20 s)	D_{p1}-U_{c10} M = 200 (20 s)	D_{p1}-U_{c25} M = 140 (14 s)
$E(\alpha'_s)$	0.63	0.59	0.8
$E(u'_s, w'_s)$	180	184	224
Number of eigenvalues necessary to reach 95% of $E(\alpha'_s)$	15	18	14
Number of eigenvalues necessary to reach 95% of $E(u'_s, w'_s)$	10	12	11
(Number of eigenvalues necessary to reach 95% of $E(\alpha'_s))/M$ [%]	7.5	9	10
(Number of eigenvalues necessary to reach 95% of $E(u'_s, w'_s))/M$ [%]	5	6	7.9

As shown in Figure 8, the ambient current seems to have a modest impact on the amount of $E(u'_s, w'_s)$ extracted for U_c values less than U_c = 15 cm/s. Then, for strong ambient currents, we observe a modification in the evolution, as $E(u'_s, w'_s)$ reaches a marked augmentation of nearly 124%. The level agitation of the solid volume phase velocities suddenly increases beyond a threshold placed between 15 and 20 cm/s. It can be inferred that, below this threshold, the resistance opposed to the strength of Uc limits the development of the agitation. Note that the evolution of $E(\alpha'_s)$ shows more marked differences. Before the threshold we observe a clear decrease, then a similar augmentation of ~124% is also reached for U_c = 20 cm/s.

Moreover, this observation completes the values of falling time (T_f) and the water–sediment mixture release diameter when the collapse occurs, as measured by Nguyen [4] for sand 1 and the different values of U_c studied in this work. This author noticed an augmentation of both values with the increase in U_c; however, this augmentation is clearly less marked when the ambient current reaches 20 cm/s.

As can be seen in Figures 9 and 10, it appears that the ambient current presence breaks the symmetry of the POD modes in all the eigenfunctions for both POD decompositions. For D_{p1}-U_{c10}, the stretching of upstream POD modes of the eigenfunctions extracted by POD_{2C} stays slight (Figure 10a). The increase in the U_c value leads to a decrease in the size of the POD modes, their gradual stretching and distortion and their displacement in the left direction. In other words, as shown in Figure 10, according to the strength of the ambient current the dynamics of the solid volume fraction can exhibit: a regime within a marked spatial organization and POD modes placed on both sides of the water–sediment mixture injection point (D_{p1}-U_{c10}), or a regime showing a heavy loss of the spatial organization of the eigenfunctions and all the POD modes placed on the left of water–sediment mixture injection point (D_{p1}-U_{c25}). The eigenfunctions extracted by POD_{2C} for different values of U_c, and not presented here, highlight that the transition between the two regimes occurs at a value between 15 and 20 cm/s. Obviously, this shape of the POD modes reflects the presence of shear observed on turbidity snapshots (cf. Figure 2c,d). Note that at the early steps of time, turbidity isocontours have regular shapes; later, when sediments evolve on the bottom, turbidity presents irregular contours. With the increase in the U_c value, the shearing and the irregularity of the turbidity contours appears at an earlier time after the sediment injection. A similar impact of an ambient current can be also observed on the

eigenfunctions obtained from POD_{1C} decomposition of the difference compared to the mean solid volume fraction snapshots. Indeed, for D_{p1}-U_{c10} (cf. Figure 9), POD modes of density transport placed downstream the point of injection of the water–sediment mixture are slightly distorted, and the deformation is more marked for upstream POD modes. These collapses and distortions are due to the resistance of the bottom to the density transport against the direction of the ambient current. It can be also shown that the POD modes placed upstream have more important intensities compared to the downstream ones. Obviously, this intensity distribution reflects that sediment is pushed by the ambient current to the left. Changes from U_c = 10 cm/s to U_c = 25 cm/s imply an amplification of the loss of the spatial organization of the solid phase volume fraction, in other words the destruction of the coherency of the particle's clouds.

Figures 9c and 10c (i.e., Figures 9d and 10d) show the POD mode outlines (solid line) superimposed to the four first eigenfunctions for D_{p1}-U_{c10} (i.e., D_{p1}-U_{c25}). As previously noticed, in all the eigenfunctions, the POD modes have been displaced to the left, pushed by the ambient current. For U_c = 25 cm/s, the higher value of ambient current studied in this paper, all the POD modes observed in both sets of eigenfunctions are strictly placed on the left of the water–sediment mixture injection point.

In spite of the displacement towards the left, the front of the density cloud and POD mode outlines observed for D_{p1}-U_{c10} (cf. Figures 9c and 10c) have strong similarities with the features found without the ambient current. A different behavior is noted for U_c = 25 cm/s, similar to the one previously shown for the D_{p2}-U_{c0} case. A lower layer of flat creeping structures (FS) extends almost as far as the main and upper structures (MS) (cf. Figure 10d). Thus, the downstream front of the particle cloud outline shows a crushing linked to the resistance of the bottom against the sediment transport. Note that the sediment plume observed in Figure 2d (t = 14 s) has a very low concentration.

4. Conclusions

In this work, numerical simulations of water–sediment mixture release were carried out according to the test conditions studied in an experimental way [1,2] and by previous numerical simulations [3,4]. The POD tool was, respectively, applied in scalar and vectorial versions, on the differences in the mean solid volume fraction snapshots and on the differences in the mean solid phase velocities fields to extract the most important pattern of their dynamics.

Two complementary POD tools were used to clarify the link between the solid phase dynamics and the particle dispersion during the three stages of the release phenomenon, and these differences were mainly due to the particle size and its weight. Moreover, the results highlight the existence of different behaviors according to the strength of the ambient current for the D_{p1} case.

During the falling time, without an ambient current, it is observed that the particle size has a modest influence on the shape of the POD modes of the most energetic eigenfunctions extracted by POD decomposition. Indeed, for D_{p2} cases, the POD modes show an elongated shape compared to the D_{p1} cases. An analysis extended to the entire release phenomenon put to the fore that the particle size and its weight affect the passive transport of the sediment. Indeed, for D_{p2} cases, the eigenfunctions extracted by POD present POD modes stretched on the bottom due to the enhancement of the opposition of the quiet water to the solid phase motion, compared to the D_{p1} case. The evolutions of the total energy information extracted by both POD decompositions reveal some information about the influence of the particle diameter. While the impact on $E(u_s', w_s')$ appears for the decomposition of the short snapshot collection limited to the falling time, the impact on $E(\alpha_s')$ appears later for longer snapshots collections covering the settling in the concentration field. Indeed, the POD_{2C} presents the advantage of revealing the trends earlier than POD1C because the settling velocity date is intrinsic to the base parameter (u_s', w_s').

The outline obtained for the solid volume fraction velocities superposed to the POD modes extracted from POD_{2C} highlight the presence of a main structure layer placed over

a second single layer of flat and creeping structures. The interaction of these two layers is different according to the particle size, and it seems to be linked to the behavior of the water–sediment mixture transport, and more particularly to the shape of the front of the particle cloud outline. Indeed, a water–sediment mixture collapse is observed for D_{p2} and, conversely, this crushing is not observed for the D_{p1} case.

Finally, the impact of the ambient current, increasing from 0 to 25 cm/s, is also explored by using both POD tools on D_{p1} snapshots. According to the strength of U_c, the total energies and the eigenfunction patterns extracted by both POD decompositions evolve. Indeed, the regime of the release phenomenon changes. For a weak ambient current, POD patterns are displaced to the left but show regular contours. For a strong ambient current, we observe an impact on the spatial organization of the POD pattern identified in the eigenfunction extracted by both decompositions. The decrease in their size and their gradual stretching and distortion reveal the loss of their spatial organization. Their complete displacement downstream of the injection point is also observed. The transition between the regime for U_c 15 and 20 cm/s is clearly identified in the curves of total energies.

In this paper, the POD_{1C} (i.e., POD_{2C}) was applied to collections of 2D snapshots with one component (i.e., two components). A 3D case could be considered, but it would need to use a different solver. In future developments, we would like to use OPENFOAM coupled with SEDFOAM to solve the full 3D case as we carried out in the case of the flow around tidal turbines [29,30]. Those simulations are sensitive and time consuming. They will be the objective of future works. In future work, further investigation could be developed for the D_{p2} case with different ambient current velocities to determine if the discrepancies observed stay or become more marked compared to the D_{p1} case.

Author Contributions: Conceptualization, A.S.C., D.H.N. and S.S.G.; methodology, A.S.C., D.H.N. and S.S.G.; software, A.S.C.; validation, A.S.C.; formal analysis, A.S.C., D.H.N. and S.S.G.; investigation, A.S.C. and S.S.G.; resources, S.S.G.; writing—original draft preparation, A.S.C., D.H.N. and S.S.G.; writing—review and editing, A.S.C., D.H.N. and S.S.G.; visualization, A.S.C.; supervision, S.S.G.; project administration, S.S.G.; funding acquisition, S.S.G. All authors have read and agreed to the published version of the manuscript.

Funding: This research received no external funding.

Data Availability Statement: Not applicable.

Acknowledgments: Part of the computational means were founded by Manche County Council.

Conflicts of Interest: The authors declare no conflict of interest. The funders had no role in the design of the study; in the collection, analyses, or interpretation of data; in the writing of the manuscript; or in the decision to publish the results.

References

1. Villaret, C.; Claude, B.; Du Rivau, J.D. *Etude Expérimentale de la Dispersion des Rejets par Clapage*; LNHE, EDF: London, UK, 1998.
2. Boutin, R. *Dragage et Rejets en Mer. Les Produits de Type Vase*; Presses de l'ENPC: Paris, France, 2000; 307p.
3. Guillou, S.; Chauchat, J.; Pham Van Bang, D.; Nguyen, D.H.; Nguyen, K.D. Simulation of the dredged sediment's release with a two-phase flow model. *Bull. Perm. Int. Assoc. Navig. Congr.* **2011**, *142*, 25–33.
4. Nguyen, D.H.; Lévy, F.; Pham Van Bang, D.; Guillou, S.; Nguyen, K.D.; Chauchat, J. Simulation of dredged sediment releases into homogeneous water using a two-phase model. *Adv. Water Resour.* **2012**, *48*, 102–112. [CrossRef]
5. Sirovich, L. Turbulence and the dynamics of coherent structures. *Q. Appl. Math.* **1987**, *5*, 561–590. [CrossRef]
6. Holmes, P.; Lumley, J.L.; Berkooz, G. *Turbulence, Coherent Structures, Dynamical Systems, and Symmetry*; Cambridge University Press: Cambridge, UK, 1996. [CrossRef]
7. Cizmas, P.G.; Palacios, A.; O'Brien, T.; Syamlal, M. Proper-orthogonal decomposition of spatio-temporal patterns in fluidized beds. *Chem. Eng. Sci.* **2003**, *58*, 4417–4427. [CrossRef]
8. Yuan, T.; Cizmas, P.G.; O'Brien, T.O. A reduced model for a bubbling fluidized bed based on proper orthogonal decomposition. *Comput. Chem. Eng.* **2005**, *30*, 243–259. [CrossRef]
9. Brenner, T.A.; Fontenot, R.L.; Cizmas, P.G.; O'Brien, T.O.; Breault, R.W. Augmented proper orthogonal decomposition for problems with moving discontinuities. *Powder Technol.* **2010**, *203*, 78–85. [CrossRef]
10. Reddy, S.R.; Freno, B.A.; Cizmas, P.G.; Gokaltun, S.; MacDaniel, D.; Dulikravich, G.S. Constrained reduced-order models based on proper orthogonal decomposition. *Comput. Methods Appl. Mech. Engrg.* **2017**, *321*, 18–34. [CrossRef]

11. Haghgoo, M.Z.; Bergstrom, D.J.; Spiteri, R.J. Analyzing dominant particle-flow structures inside a bubbling fluidized bed. *Int. J. Heat Fluid Flow* **2019**, *77*, 232–241. [CrossRef]
12. Li, X.; Hu, B.X. Proper orthogonal decomposition reduced model for mass transport in heterogeneous media. *Stoch. Environ. Res. Risk. Assess* **2013**, *27*, 1181–1191. [CrossRef]
13. Li, X.; Chen, X.; Hu, B.X.; Navon, M.I. Model reduction of a coupled numerical model using proper orthogonal decomposition. *J. Hydrol.* **2013**, *507*, 227–240. [CrossRef]
14. Vermeulen, P.T.M.; Heemink, A.W.; Te Stroat, C.B.M. Reduced models for linear groundwater flow models using empirical orthogonal functions. *Adv. Water Resour.* **2004**, *27*, 57–69. [CrossRef]
15. Vermeulen, P.T.M.; Heemink, A.W.; Valstar, J.R. Inverse modeling of groundwater flow using model reduction. *Water Resour. Res.* **2005**, *41*, W06003. [CrossRef]
16. Polansky, J.; Wang, M. Proper Orthogonal Decomposition as a technique for identifying two-phase flow pattern based on electrical impedance tomography. *Flow Meas. Instrum.* **2017**, *53*, 126–132. [CrossRef]
17. Olbrich, M.; Bar, M.; Oberleithner, K.; Schmelter, S. Statistical characterization of horizontal slug flow using snapshot proper orthogonal decomposition. *Int. J. Multiph. Flow* **2021**, *134*, 103453. [CrossRef]
18. Munir, S.; Israr, M.; Heikal, M.R.; De Sercey, G. Identification of dominant structures and their flow dynamics in the turbulent two-phase flow using POD technique. *J. Mech. Sci. Technol.* **2015**, *29*, 4701–4710. [CrossRef]
19. Munir, S.; Farooq, U. POD based on vorticity: Application in a two-phase slog flow. *J. Fluids Eng.* **2022**, *144*, 041501. [CrossRef]
20. Munir, S.; Azis, A.R.A.; Heikal, M.R.; Israr, M. Combination of linear stochastic estimation and proper orthogonal decomposition: Application in two-phase slug flow. *J. Braz. Soc. Mech. Sci. Eng.* **2023**, *45*, 112. [CrossRef]
21. Nguyen, D.H.; Guillou, S.; Hien, L.T.T.; Nguyen, Q.H. Proper orthogonal decomposition of a very high concentrated release of sediment in water: Spatio temporal patterns. *IJRTE* **2019**, *8*, 2347–2353. [CrossRef]
22. Guillou, S.; Thiébot, J.; Chauchat, J.; Verjus, R.; Besq, A.; Nguyen, D.H.; Pouv, K.S. The Filling Dynamics of an Estuary: From the Process to the Modelling. In *Sediment Transport in Aquatic Environments*; Manning, A., Ed.; InTech: London, UK, 2011; pp. 125–146. ISBN 978-953-307-586-0. Available online: https://www.intechopen.com/chapters/20914 (accessed on 3 October 2011).
23. Barbry, N.; Guillou, S.; Nguyen, K.D. Une approche diphasique pour le calcul du transport sédimentaire en milieux estuariens. *Comptes Rendus De L'académie Des Sci.* **2000**, *328*, 793–799. [CrossRef]
24. Chauchat, J.; Guillou, S. On turbulence closures for two-phase sediment-laden flows models. *J. Geophys. Res.* **2008**, *113*, C11017. [CrossRef]
25. Nguyen, K.D.; Guillou, S.; Chauchat, J.; Barbry, N. A two-phase numerical model for suspended-sediment transport in estuaries. *Adv. Water Resour.* **2009**, *32*, 1187–1196. [CrossRef]
26. Lundgren, T. Slow flow through stationary random beds and suspensions of spheres. *J. Fluid. Mech.* **1972**, *51*, 273–299. [CrossRef]
27. Graham, A.L. On the viscosity of suspensions of solid spheres. *Appl. Sci. Res.* **1981**, *37*, 275–286. [CrossRef]
28. Farout-Fréson, I.; Sergent, P.; Lefrançois, E.; Datt, G. Modèle numérique de clapage–phase de chute. In Proceedings of the IXèmes Journées Nationales Génie Civil—Génie Côtier, Brest, France, 12–14 September 2006; pp. 179–186. [CrossRef]
29. Khaled, F.; Guillou, S.S.; Méar, Y.; Hadri, F. Impact of blockage ratio on the transport of sediments in the presence of a hydrokinetic turbine: Numerical modelling of the interaction sediments-turbine. *Int. J. Sediment Res.* **2021**, *36*, 696–710. [CrossRef]
30. Khaled, F.; Guillou, S.S.; Méar, Y.; Hadri, F. Numerical investigation of the local impact of hydrokinetic turbine on sediment transport—Comparison between two actuator models. *Eur. J. Mech. B Fluids* **2023**, *102*, 31–45. [CrossRef]